



# Axonal Ensheathment in the Nervous System of Lamprey: Implications for the Evolution of Myelinating Glia

Marie-Theres Weil,<sup>1,2</sup> Saskia Heibeck,<sup>1</sup> Mareike Töpperwien,<sup>3</sup> Susanne tom Dieck,<sup>4</sup> Torben Ruhwedel,<sup>1</sup> Tim Salditt,<sup>2,3</sup> María C. Rodicio,<sup>5</sup> Jennifer R. Morgan,<sup>6</sup>  Klaus-Armin Nave,<sup>1,2</sup> Wiebke Möbius,<sup>1,2</sup> and  Hauke B. Werner<sup>1</sup>

<sup>1</sup>Department of Neurogenetics, Max Planck Institute of Experimental Medicine, 37075 Göttingen, Germany, <sup>2</sup>Center for Nanoscale Microscopy and Molecular Physiology of the Brain, Göttingen, Germany, <sup>3</sup>Institute for X-Ray Physics, Georg August University, 37077 Göttingen, Germany, <sup>4</sup>Synaptic Plasticity Department, Max Planck Institute for Brain Research, 60438 Frankfurt, Germany, <sup>5</sup>Department of Cell Biology, University of Santiago de Compostela, 15782 Santiago de Compostela, Spain, and <sup>6</sup>Eugene Bell Center for Regenerative Biology and Tissue Engineering, Marine Biological Laboratory, Woods Hole, Massachusetts 02543

In the nervous system, myelination of axons enables rapid impulse conduction and is a specialized function of glial cells. Myelinating glia are the last cell type to emerge in the evolution of vertebrate nervous systems, presumably in ancient jawed vertebrates (gnathostomata) because jawless vertebrates (agnathans) lack myelin. We have hypothesized that, in these unmyelinated species, evolutionary progenitors of myelinating cells must have existed that should still be present in contemporary agnathan species. Here, we used advanced electron microscopic techniques to reveal axon–glia interactions in the sea lamprey *Petromyzon marinus*. By quantitative assessment of the spinal cord and the peripheral lateral line nerve, we observed a marked maturation-dependent growth of axonal calibers. In peripheral nerves, all axons are ensheathed by glial cells either in bundles or, when larger than the threshold caliber of 3  $\mu\text{m}$ , individually. The ensheathing glia are covered by a basal lamina and express *SoxE*-transcription factors, features of mammalian Remak-type Schwann cells. In larval lamprey, the ensheathment of peripheral axons leaves gaps that are closed in adults. CNS axons are also covered to a considerable extent by glial processes, which contain a high density of intermediate filaments, glycogen particles, large lipid droplets, and desmosomes, similar to mammalian astrocytes. Indeed, by *in situ* hybridization, these glial cells express the astrocyte marker *Aldh1l1*. Specimens were of unknown sex. Our observations imply that radial sorting, ensheathment, and presumably also metabolic support of axons are ancient functions of glial cells that predate the evolutionary emergence of myelin in jawed vertebrates.

**Key words:** axon–glia interaction; electron microscopy; myelin; oligodendrocyte; radial sorting; Schwann cell

## Significance Statement

We used current electron microscopy techniques to examine axon–glia units in a nonmyelinated vertebrate species, the sea lamprey. In the PNS, lamprey axons are fully ensheathed either individually or in bundles by cells ortholog to Schwann cells. In the CNS, axons associate with astrocyte orthologs, which contain glycogen and lipid droplets. We suggest that ensheathment, radial sorting, and metabolic support of axons by glial cells predate the evolutionary emergence of myelin in ancient jawed vertebrates.

## Introduction

Most fast-transmitting axons in jawed vertebrates (gnathostomata) are myelinated; that is, insulated with multiple compacted layers of plasma membrane of oligodendrocytes in the

CNS and Schwann cells in the PNS (Nave and Werner, 2014). Myelin sheaths accelerate nerve conduction 20- to 100-fold compared with unmyelinated axons of the same diameter (Castelfranco and Hartline, 2016) by facilitating saltatory action potential propagation (Tasaki, 1939). Jawless vertebrates (agnatha/cyclostomata) including lamprey do not possess myelin (Bullock et al., 1984) and thus represent an ancestral stage in vertebrate nervous system evolution (for phylogenetic relation-

Received April 23, 2018; revised May 29, 2018; accepted June 6, 2018.

Author contributions: M.-T.W., K.-A.N., W.M., and H.B.W. edited the paper; M.-T.W., W.M., and H.B.W. designed research; M.-T.W., S.H., M.T., and T.R. performed research; M.C.R. and J.R.M. contributed unpublished reagents/analytic tools; M.-T.W., S.H., S.t.D., T.S., K.-A.N., W.M., and H.B.W. analyzed data; H.B.W. wrote the paper.

This work was supported by the Cluster of Excellence and Deutsche Forschungsgemeinschaft (DFG) Research Center Nanoscale Microscopy and Molecular Physiology of the Brain (M.-T.W., K.-A.N., T.S., and W.M.), the DFG (Grants WE 2720/2-2 and WE 2720/4-1 to H.B.W.), and the European Research Council (Advanced Grant to K.-A.N.). We thank C. Nardis, A. Steyer, and K. Hanslik for technical support.

The authors declare no competing financial interests.

Correspondence should be addressed to either Wiebke Möbius or Hauke B. Werner, Max Planck Institute of Experimental Medicine, Hermann-Rein-Str. 3, D-37075 Göttingen, Germany, E-mail: Moebius@em.mpg.de or Hauke@em.mpg.de.

DOI:10.1523/JNEUROSCI.1034-18.2018

Copyright © 2018 the authors 0270-6474/18/386586-11\$15.00/0

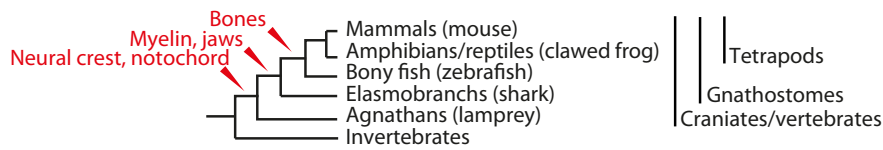


**Figure 1.** Evolutionary relationships of species groups and representative model species discussed in the present study. Consequential evolutionary innovations are indicated (red arrowheads). (Figure adapted with permission from Schweitzer et al., 2006; Grillner and Robertson, 2016; and Salzer and Zalc, 2016).

ships, see Fig. 1). Clustering of sodium channels to generate action potentials at axon initial segments evolved before the divergence of jawed and jawless vertebrates ~560 million years ago (MYA) (Hill et al., 2008). Conversely, the anchor motifs that

cluster potassium channels at nodes of Ranvier evolved exclusively in the gnathostomata line (Hill et al., 2008) at approximately the same time as myelin (Zalc et al., 2008) >420 MYA ago (King et al., 2017).

In addition to myelination, glial cells guide neurodevelopment (Marin et al., 2010) and provide metabolic support to axons (Fünfschilling et al., 2012; Lee et al.,

2012; Beirowski et al., 2014; Volkenhoff et al., 2015; Liu et al., 2017). Indeed, glial cells ensheath axons in species ranging from mice to flies (Banerjee and Bhat, 2008; Freeman, 2015; Schirmeier

**Table 1. Presence of glial marker gene homologs in the sea lamprey genome**

Gene ID (mouse)	Gene name (mouse)	Swisprot ID (mouse)	Closest relative in lamprey <sup>a</sup>	Mouse ortholog <sup>b</sup>	
<b>Schwann cell lineage</b>					
TF markers	<i>Egr2</i>	Early growth response 2/Krox20	EGR2_MOUSE	S4RIV4_PETMA	EGR1/KROX24
	<i>Pou3f1</i>	POU domain class 3 TF 1/Oct6	PO3F1_MOUSE	S4RID7_PETMA	POU2F1/OCT1
	<i>Sox8</i>	SRY-box TF 8	SOX8_MOUSE	SOXE1 <sup>c</sup>	SOX8
	<i>Sox9</i>	SRY-box TF 9	SOX9_MOUSE	SOXE3 <sup>c</sup>	SOX9
	<i>Sox10</i>	SRY-box TF 10	SOX10_MOUSE	SOXE2 <sup>c</sup>	SOX10
Other markers	<i>Mpz</i>	Myelin protein zero/PO	MYPO_MOUSE	S4RAD2_PETMA	MPZL3
	<i>Pmp2</i>	Peripheral myelin protein 2/Fabp8	MYP2_MOUSE	S4R6S2_PETMA	FABP3
	<i>Pmp22</i>	Peripheral myelin protein 22kDa	PMP22_MOUSE	S4RZM8_PETMA/PMP22B	PMP22
	<i>Prx</i>	Periaxin	PRAX_MOUSE	No hit found	n/a
<b>Astrocyte lineage</b>					
TF markers	<i>Gli1/2/3</i>	GLI family zinc finger 1/2/3	GLI1_MOUSE	S4RTN6_PETMA	GLI3
	<i>Hes5</i>	Hairy and enhancer of split 5	HES5_MOUSE	S4R8M4_PETMA	HES1
	<i>Sox2</i>	SRY-box TF 2	SOX2_MOUSE	S4RZR4_PETMA/SOXB1/SOX2 <sup>d</sup>	SOX2
	<i>Sox9</i>	SRY-box TF 9	SOX9_MOUSE	SOXE3 <sup>c</sup>	SOX9
Other markers	<i>Aldh11</i>	Aldehyde dehydrogenase 1 family, member L1	AL1L1_MOUSE	S4RGV7_PETMA	ALDH1L1 (Figure 5E)
	<i>Aqp4</i>	Aquaporin 4	AQP4_MOUSE	S4RUM3_PETMA	AQP4
	<i>Fgfr3</i>	Fibroblast growth factor receptor 3	FGFR3_MOUSE	S4RS21_PETMA	FGFR2
	<i>Gfap</i>	Glial fibrillary acidic protein	GFAP_MOUSE	S4RE82_PETMA	VIM
	<i>Gjb6</i>	Gap junction protein beta 6/Connexin CX30	CXB6_MOUSE	S4RXA7_PETMA/Connexin 27.5	GJB1/CX32
	<i>Slc1a2</i>	Solute carrier family 1 member 2 (glutamate transporter GLT-1)	EAA2_MOUSE	S4RZS9_PETMA1	SLC1A2
	<i>Slc1a3</i>	Solute carrier family 1 member 2 (glutamate transporter GLAST)	EAA1_MOUSE	S4R7G6_PETMA	SLC1A4
<b>Oligodendrocyte lineage</b>					
TF markers	<i>Myrf</i>	Myelin regulatory factor	MYRF_MOUSE	No hit found <sup>e</sup>	n/a
	<i>Nkx6-2</i>	NK6 homeobox TF 2	D3Z4R4_MOUSE	S4RC35_PETMA	HMX2/NKX5-2
	<i>Olig1</i>	Oligodendrocyte TF 1	OLIG1_MOUSE	S4RSW9_PETMA	NeuroD1
	<i>Olig2</i>	Oligodendrocyte TF 2	OLIG2_MOUSE	S4RNM7_PETMA	NeuroD1
	<i>Sox10</i>	SRY-box TF 10	SOX10_MOUSE	SOXE2 <sup>c</sup>	SOX10
Other markers	<i>Cnp</i>	Cyclic nucleotide phosphodiesterase	CN37_MOUSE	S4RC98_PETMA/CNP	CNP
	<i>Cldn11</i>	Claudin 11	CLD_11	S4RJV3_PETMA	CLDN10
	<i>Cspg4</i>	Chondroitin sulfate proteoglycan 4/NG2	CSPG4_MOUSE	S4RBJ2_PETMA	CSPG4/NG2
	<i>Mag</i>	Myelin associated glycoprotein	MAG_MOUSE	S4RQL3_PETMA	PXDN
	<i>Mbp/Golli</i>	Myelin basic protein (MBP)/Gene of oligodendrocyte lineage (GOLLI) transcription unit	MBP_MOUSE	No hit found for MBP; Only GOLLI <sup>f</sup>	GOLLI
	<i>Mobp</i>	Myelin-associated oligodendrocyte basic protein	MOBP_MOUSE	No hit found	n/a
	<i>Mog</i>	Myelin oligodendrocyte glycoprotein	MOG_MOUSE	No hit found	n/a
	<i>Opalin</i>	Opalin/TMEM10	OPALI_MOUSE	No hit found	n/a
	<i>Pdgfra</i>	Platelet derived growth factor receptor alpha	PGFRA_MOUSE	S4RQ64_PETMA	KDR/VEGFR2
	<i>Plp1</i>	Proteolipid Protein	MYPR_MOUSE	S4RCY1_PETMA	GPM6B
	<i>Tspan2</i>	Tetraspanin 2	TSN2_MOUSE	S4RU78_PETMA	TSPAN9

Known markers for Schwann cells, astrocytes, and oligodendrocytes were blasted at ensembl.org against the *P. marinus* somatic genome (release version 7.0) to identify the closest relative in lamprey.

<sup>a</sup>Given are Swisprot/Uniprot ID, protein name (if assigned), and a prior publication if available.

<sup>b</sup>Identified lamprey proteins were then blasted against all mouse proteins; given is the protein name.

<sup>c</sup>McCaughey and Bronner-Fraser (2006).

<sup>d</sup>Cattell et al. (2012).

<sup>e</sup>A fragment ortholog to *Myrf* was detected previously in the genome of Japanese lamprey (*Lethenteron japonicum*) (Li and Richardson, 2016).

<sup>f</sup>Werner (2013).

TF, Transcription factor; n/a, not applicable

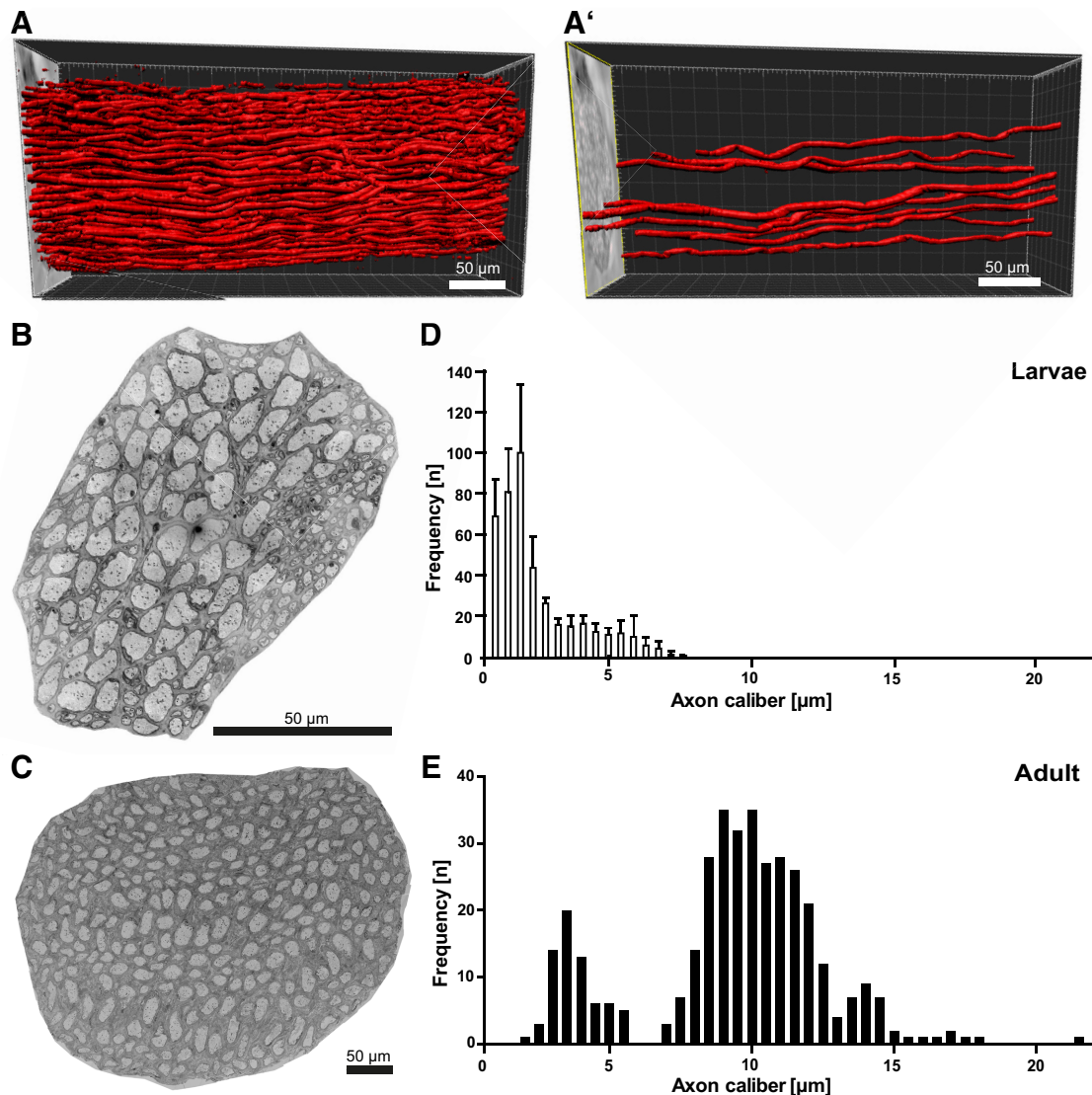


**Figure 2.** Spatial organization and maturation-dependent radial growth of peripheral lamprey axons. *A*, X-ray tomography of an adult lamprey LLN over a length of 370  $\mu\text{m}$ . 3D reconstruction visualizes numerous large-caliber axons. *A'*, Representative axons selected from *A*. *B*, *C*, Scanning electron micrographs of cross-sectioned LLN in larval (*B*) and adult (*C*) lamprey. Note the different scale bar sizes. *D*, *E*, Calibers of individual axons in entire larval (*D*) and adult (*E*) LLNs indicating maturation-dependent radial growth. Data are shown as mean and SD.  $n = 1675$  axons in 2 larvae;  $n = 373$  axons in 1 adult.

et al., 2016). However, knowledge remained limited about the structure of axon–glia units and the evolutionary progenitors of myelinating glia at the root of the vertebrate line. However, mining of genomic datasets allows only limited conclusions about cellular structures (Werner, 2013; Table 1) and ultimately requires consideration in conjunction with morphological analyses.

The agnathan species most commonly investigated regarding nervous system evolution is the sea lamprey, *Petromyzon marinus* (Sugahara et al., 2017). Lamprey is also a valuable model for investigating embryonic development (Sugahara et al., 2011; Green et al., 2017; Martik and Bronner, 2017), synaptic function (Morgan et al., 2004; Brodin and Shupliakov, 2006; Gerachshenko et al., 2009), locomotion (Mullins et al., 2011; Grillner and El Manira, 2015), and injury and regeneration (Cornide-Petronio et al., 2011; Busch and Morgan, 2012; Lau et al., 2013; Fernández-López et al., 2014; Rasmussen and Sagasti, 2017). Recently, whole-genome sequencing further increased its value as a model species (Smith et al., 2013), for example, by facilitating *in*

*situ* hybridization with cell-type-specific markers. When the lamprey nervous system was analyzed previously by conventional electron microscopy, some axons were noted to possess cellular ensheathment (Schultz et al., 1956; Peters, 1960; Bertolini, 1964; Bullock et al., 1984; Rovainen and Dill, 1984; Lurie et al., 1994; Fraher, 2002; Gelman et al., 2009). However, focusing on other aspects, most studies noted glial ensheathment on the side.

Electron microscopic visualization of nervous tissue morphology has benefited from recent technical advances, in particular with respect to tissue fixation (a frequent difficulty when analyzing aquatic species), but also contrast and 3D visualization. Here, we investigated the structural organization of axon–glia units in lamprey using optimized sample preparation and current visualization techniques. We used X-ray phase-contrast tomography (Bartels et al., 2015) to assess tissue en bloc in 3D at low resolution, focused ion beam–scanning electron microscopy (FIB-SEM) (Knott et al., 2008; Schertel et al., 2013) to visualize the spatial relationships of cells and their processes in 3D and SEM to approach large tissue sections at high resolution. The

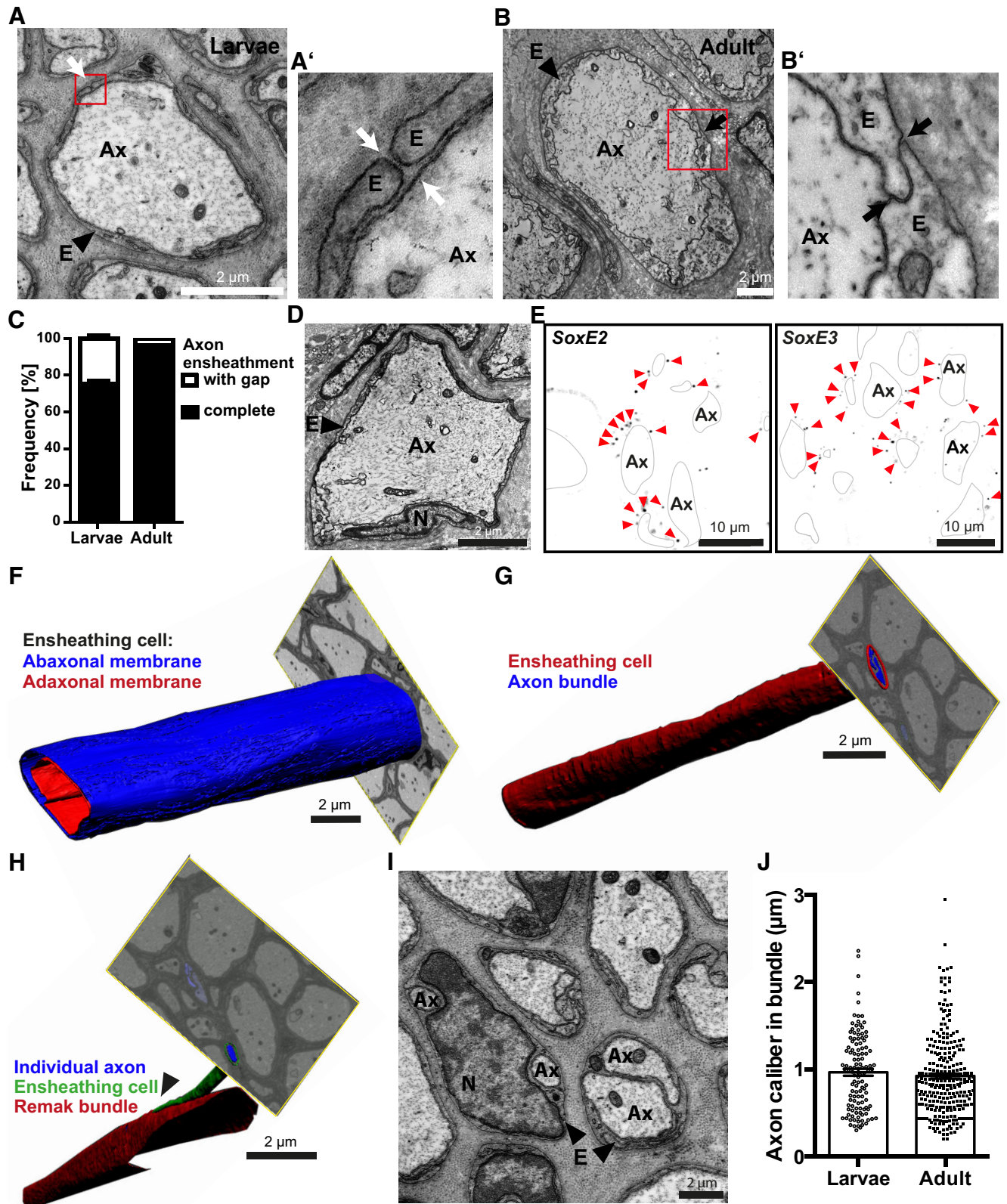


**Figure 3.** Axonal ensheathment by Schwann cell orthologs in the lamprey PNS. **A, B**, Electron micrographs of a cross-sectioned LLN in larval (**A**) and adult (**B**) lamprey. Note the glial ensheathment (**E**) of axons (**Ax**). Red boxes indicate areas magnified in **A'** and **B'**, respectively. **A', B'**, Axonal ensheathment occasionally displayed gaps (**A'**) in larval but was closed (**B'**) in adult lamprey. **C**, Quantification of gapped and closed axonal ensheathment in entire cross-sectioned LLNs. Note the maturation-dependent closure of ensheathment gaps. Data are shown as mean and SD.  $n = 787$  axons in 2 larvae;  $n = 343$  axons in 1 adult. **D**, Electron micrograph of an axon (**Ax**) in the cross-sectioned adult LLN highlighting an ensheathing cell nucleus (**N**). **E**, FISH of a cross-sectioned LLN detecting *Sox2* and *Sox3*, the lamprey orthologs of *Sox9* and *Sox10*, respectively. Note that *Sox2* and *Sox3*-labeling (pseudocolor representation by black puncta marked by arrowheads) partially outlines axons (**Ax**, black lines). **F–H**, FIB-SEM micrographs and 3D reconstruction. **F**, Adaxonal (red) and abaxonal (blue) plasma membrane of a representative cell ensheathing an individual axon in the larval LLN. Note the structural homogeneity over at least  $20\ \mu\text{m}$ . See also Movie 1. **G**, Bundle of multiple axons (blue) ensheathed by a single ensheathing cell (red) showing homogeneity over at least  $20\ \mu\text{m}$ . See also Movie 2. **H**, As an anecdotal observation, an axon (blue) with its individual ensheathment (green) leaves a bundle of (Figure legend continues.)

latter allows quantitative morphological scrutiny of sections of entire nerves or spinal cords (SCs). Our observations support the concept that glial cells associate with axons to provide metabolic support, a function that predates the evolutionary emergence of myelin.

## Materials and Methods

**Animals.** Larval sea lampreys *P. marinus* (premetamorphic ammocoetes; approximate body length 12 cm; estimated age 5–7 years;  $n = 2$ ) were obtained from the Marine Biological Laboratory (Woods Hole, MA). An adult prespawning upstream migrating sea lamprey (approximate body length 80 cm; estimated age 7–9 years;  $n = 1$ ) was acquired at a local fish market (Santiago de Compostela, Spain). Animals were of unknown sex. Body pieces were fixed in 4% PFA in phosphate buffer (PB) containing 109.5 mM  $\text{NaH}_2\text{PO}_4 \cdot \text{H}_2\text{O}$ , 93.75 mM  $\text{Na}_2\text{HPO}_4 \cdot 2\text{H}_2\text{O}$ , and 86.2 mM NaCl for 1 h at room temperature (RT) and stored in PB until used.

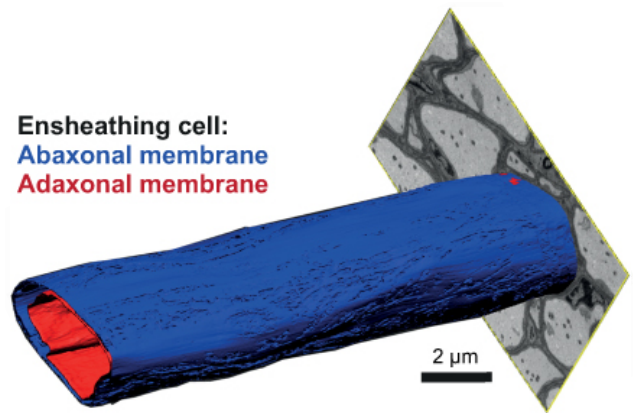
**Sequence analysis.** The indicated sequences were retrieved from the databases Swiss-Prot/Uniprot ([www.uniprot.org](http://www.uniprot.org)) and NCBI (<https://ncbi.nlm.nih.gov>). Sequence alignments for prediction of evolutionary relationships were performed with Lasergene Megalign software using Clustal W standard slow accurate parameters and protein weight matrix Gonnet250.

**FISH.** FISH procedures with single-molecule sensitivity for low copy mRNA targets (Will et al., 2013) were used to detect *Aldh11l1*, *SoxE1*, *SoxE2* and *SoxE3* mRNA in lamprey. Lateral line nerves (LLNs) or SCs were dissected, postfixed in 4% PFA in DEPC-treated PBS (1 h at RT), infiltrated stepwise with sucrose, cryosectioned at 10  $\mu\text{m}$  thickness, and mounted onto slides (Ultrafrost Plus; Thermo Fisher). Slides were transferred into incubation chambers (Secure-Seal; Thermo Fisher). In the chambers, sections were postfixed for 10 min in 4% PFA in DEPC-treated PBS. *In situ* hybridization was then performed using the QuantiGene ViewRNA kit (Thermo Fisher) according to the manufacturer's instructions using probe sets specific for lamprey *SoxE1* (GenBank accession no. AY830453), *SoxE2* (DQ328983), *SoxE3* (DQ328984), and *Aldh11l1* (CAAA18610) mRNAs (Thermo Fisher). A probe set for *E. coli Kd12* mRNA was used as a negative control. Briefly, sections were permeabilized for 10 min in detergent solution, washed, and hybridized with the specific probe sets diluted 1:100 for 3–16 h at 40°C. After washing, samples were hybridized consecutively with preamplification oligonucleotides, amplification oligonucleotides, and finally label oligonucleotides conjugated with a fluorescent dye emitting at 550 nm. All oligonucleotide sets were used 1:100 at 40°C for 1 h with extensive washing between steps. Samples were imaged on a Leica SP5 confocal microscope. For quantification of *Aldh11l1*-positive cells in the SC,  $n = 198$  nuclei on two sections were analyzed with respect to the number of labeling puncta per DAPI-positive cell; cells were judged as *Aldh11l1* positive if they displayed  $\geq 3$  labeling puncta in close proximity to the nucleus.

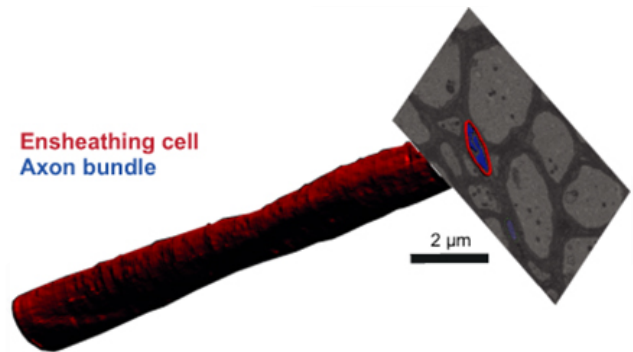
**Electron microscopy.** Dissected body pieces, SCs, and LLNs were postfixed in 4% PFA and 2.5% glutaraldehyde in 0.1 M PB containing 109.5 mM  $\text{NaH}_2\text{PO}_4 \cdot \text{H}_2\text{O}$ , 93.75 mM  $\text{Na}_2\text{HPO}_4 \cdot 2\text{H}_2\text{O}$ , and 86.2 mM NaCl for at least 24 h. To achieve sufficient contrast for imaging backscattered electrons by SEM, tissue samples were processed using a modified protocol of the reduced osmium-thiocarbohydrazide-osmium method (Deerinck et al., 2010) as described previously (<https://ncmir.ucsd.edu/sbem-protocol>). The samples were washed in 0.1 M PB buffer ( $3 \times 15$  min) and then incubated for 3 h at 4°C in 2%  $\text{OsO}_4$  and 0.25%  $\text{K}_4[\text{Fe}(\text{CN})_6]$  to reduce the  $\text{OsO}_4$  to  $\text{OsO}_2$ . After washing with  $\text{ddH}_2\text{O}$ , the samples were incubated with 0.1% thiocarbohydrazide (in  $\text{ddH}_2\text{O}$ ) (1 h at RT). To contrast the samples, they were treated with 2%  $\text{OsO}_4$  (90 min). After washing with  $\text{ddH}_2\text{O}$ , the samples were contrasted overnight at 4°C with 2.5% uranyl acetate, followed by several washes with  $\text{ddH}_2\text{O}$ .

←

(Figure legend continued.) multiple axons (red). *I*, Electron micrograph of a LLN highlighting bundles of two or more axons (Ax). For quantification of axons per bundle, see Figure 4. E, Ensheathing cell; N, nucleus. *J*, Calibers of LLN axons ensheathed in bundles. Data are shown as mean and SEM.  $n = 120$  axons in 2 larvae;  $n = 274$  axons in 1 adult.



**Movie 1.** Ensheathment of an individual axon in the LLN. Electron micrographs gained by FIB-SEM and 3D reconstruction highlighting the adaxonal (red) and abaxonal (blue) plasma membrane of a representative cell ensheathing an individual axon in the larval LLN. For preview image, see Figure 3F.



**Movie 2.** Ensheathment of a bundle of multiple axons in the LLN. FIB-SEM and 3D reconstruction highlighting a bundle of multiple axons (blue) ensheathed by a single ensheathing cell (red). As an anecdotal observation, an axon (blue) with its individual ensheathment (green) leaves a bundle of multiple axons (red). For preview images, see Figure 3, G and H.



Then, the samples were dehydrated in an increasing ethanol series (15 min each at 4°C; 30%, 50%, 70%, and 90% ethanol; then  $4 \times 100\%$  acetone). Subsequently, the samples were infiltrated with increasing concentrations of Durcupan resin (Sigma-Aldrich) (2 h each at RT; 25%, 50%, 75% Durcupan in acetone) and then incubated in 100% Durcupan overnight. Fresh Durcupan with accelerator (Durcupan component D) was added the next day for 5 h before embedding in gelatin capsules or flat embedding molds. The resin was polymerized for 48 h at 60°C.

Semithin sections at 500 nm thickness were cut and stained with methylene blue and Azure II (Richardson et al., 1960) for 1–2.5 min before observation using an epifluorescence light microscope (Axiophot; Zeiss). Ultrathin sections were cut at 50 nm thickness and transmission electron micrographs were obtained with the Zeiss EM900 or Zeiss EM912 AB equipped with a 2k-CCD camera (TRS). For scanning electron micrographs, 100-nm-thick sections were cut and transferred to a  $\text{H}_2\text{SO}_4$ -washed silicon wafer using a self-made stainless steel loop. The sections were left to dry at 60°C on a warm plate. The wafer was then sputter coated with 4 nm carbon before imaging using a FIB-SEM (Crossbeam 540; Zeiss). The tissue sections were imaged at 1.2 kV with 5 nm pixel size and at least 10  $\mu\text{s}$  dwell time using the energy selective backscattered detector.

Images were analyzed using Fiji (Fiji.sc). Axonal caliber ( $c$ ) was calculated from the measured area ( $A$ ) using the equation  $c = 2\sqrt{(A/\pi)}$ .

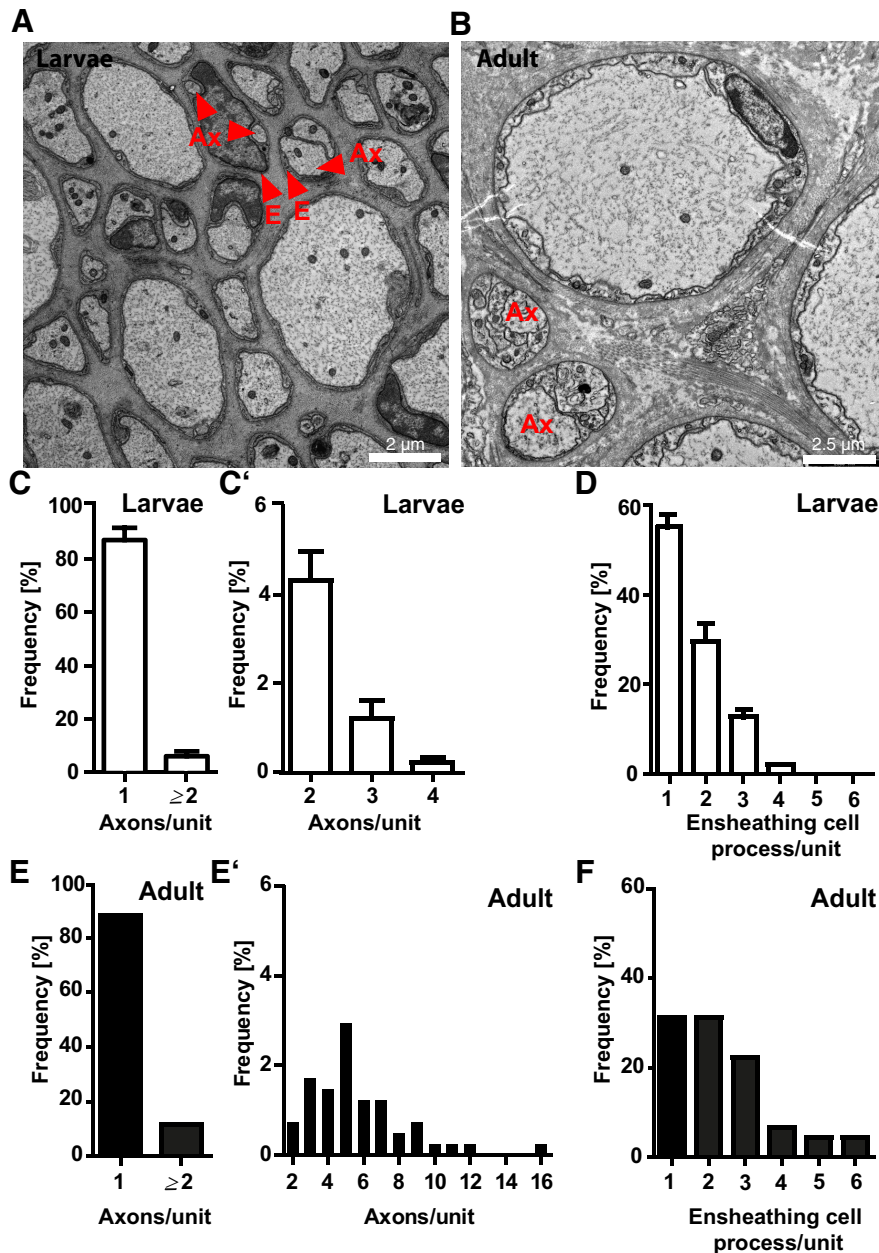


**Figure 4.** Numbers of axons and glial processes per bundle in the lamprey PNS. *A, B*, Electron micrographs of LLNs in larval (*A*) and adult (*B*) lamprey to exemplify axons in bundles (arrowheads) or with multiple ensheathing cell processes (Ax). *C, C', E, E'*, Frequencies of axons per bundle in the entire LLN of larval (*C, C'*) and adult (*E, E'*) lamprey. *C, E*, Percentage of individually ensheathed axons; that is, axon/ensheathing cell units containing one axon versus units containing several axons. *C', E'*, Subdivision of the numbers of axons in axon/ensheathing cell-units containing  $\geq 2$  axons. Note the maturation-dependent increase in the number of axons per bundle. *D, F*, Frequencies of ensheathing cell processes per bundle in the entire LLN of larval (*D*) and adult (*F*) lamprey. Data are shown as mean and SD.  $n = 1675$  axons in 2 larvae;  $n = 411$  axons in 1 adult.

Frequency distributions of axonal calibers were calculated for entire LLNs or the indicated SC regions. For the coverage of axons by astrocytes, axonal circumference and the portion covered by glial processes were measured in Fiji. From these values, the percentage of coverage was calculated. Distances between ensheathing cell nuclei were measured from longitudinal sections of the LLN.

For volume imaging, the samples were trimmed around the area of interest in the dorsal SC or the LLN, polymerized for 5 d, and sputter coated with 10 nm platinum. The block face was exposed by milling a coarse trench of  $60 \mu\text{m}$  with the focused ion beam. The region of interest was selected and then the serial block face milling and imaging process was set up using the ATLAS3D software (Zeiss), including platinum and

carbon pad deposition on top of the block surface. After fine polish of the block surface, the block face imaging over  $\sim 30 \mu\text{m}$  was started with the following settings: 5 nm pixel size, 12  $\mu\text{s}$  dwell time, and 1.2 kV. The resulting image stack was preprocessed by aligning, binning, and enhancing the local contrast. The structures of interest were mainly segmented manually in Microscopy Image Browser (Electron Microscopy Unit, University of Helsinki, Finland) and the 3D reconstruction was visualized in Imaris (Bitplane, University of California–Santa Barbara).

**X-ray tomography.** Tomographic measurements were performed at the GINIX setup installed at the beamline P10 of the PETRA III storage ring at DESY (Hamburg) (Salditt et al., 2015). The setup was operated at 13.8 keV in the holographic imaging mode with a waveguide as a beam-refining optic (Krüger et al., 2012). In this mode, phase and therefore density information of the sample is encoded in intensity modulations of the X-ray beam via free-space propagation behind the object. The detection system was a scintillator-based fiber-optic-coupled sCMOS camera with a  $15 \mu\text{m}$  gadox scintillator and a pixel size of  $6.5 \mu\text{m}$  (Photonic Science). Due to the cone beam geometry of the setup, the effective pixel size can be varied by changing the geometrical magnification of the setup (Krenkel et al., 2015). In this case, the source-to-object distance was set to 145 mm and the source-to-detector distance to 5.05 m, leading to a magnification of  $\sim 35$  and an effective pixel size of 186 nm. For the tomographic measurements, 1001 projections  $>180^\circ$  were recorded at 4 propagation distances with an exposure time of 0.5 s per projection. Multiple distances were necessary to properly reconstruct the phase information of the single projections using a CTF-based approach (Bartels et al., 2015). The herein defined regularization parameters, denoted as in (Bartels et al., 2015), were set to  $\kappa = 40$  and  $\alpha_2 = 0$  based on visual inspection. After the phase retrieval, tomographic reconstruction was subsequently performed with the MATLAB-implemented iradon function using a standard Ram-Lak filter. The axons were segmented in Microscopy Image Browser and visualized in 3D using Imaris.

**Experimental design and statistical analysis.** Numbers and specifications of animals used for the analysis are given in the “Animals” section. For all quantifications,  $n$  numbers are specified in the respective figure legends. Where appropriate, data represent mean with SD for quantifications in larval lampreys and mean for quantifications in adult lamprey. Frequency distributions of axonal calibers were assessed using the Kolmogorov–Smirnov test; the results of this statistical assessment are given in the Results section.

## Results

To visualize the spatial organization of axons in the PNS of a nonmyelinated vertebrate species, we subjected a segment of the LLN dissected from an adult sea lamprey (*P. marinus*) to X-ray tomography. It was possible to reconstruct numerous large-caliber axons over a length of  $370 \mu\text{m}$  in 3D (Fig. 2*A*). Within this segment, the observed axons largely

run in parallel; however, moderate axonal bending was observed (Fig. 2A'). At higher resolution, SEM allowed assessing all axons in entire cross-sectioned LLNs (Fig. 2B,C). Noticeably, the adult LLN is approximately four times larger than larval nerves, reflecting maturation-dependent growth. The frequency distribution of the calibers of all individual LLN axons is shifted toward large calibers in adult compared with larval LLNs (Fig. 2D,E; Kolmogorov–Smirnov test  $p < 0.0001$ ), whereas the total number of axons remains largely similar. Most LLN axons undergo intense maturation-dependent radial growth.

In our electron microscopic analysis, we noted that all individual LLN axons are ensheathed by glial cells (Fig. 3A,B). The ensheathment of some axons contained small gaps in larval nerves (Fig. 3A'), but was generally closed (Fig. 3B') in adult nerves (Fig. 3C). This implies maturation-dependent closure of the glial ensheathment. All axon–glia units were covered by a basal lamina.

Considering the remarkably close association between peripheral axons and ensheathing cells, we further examined the cellular morphology. The periaxonal space between the axonal surface and the adaxonal surface of ensheathing glia was small and regular and comprised electron-dense material, implying the presence of extracellular proteins. The cytoplasm of the ensheathing cells constitutes one thin layer of irregular width, which contains cellular compartments including nuclei (Fig. 3D). In no case did the cytoplasm display myelin-like compaction. When scrutinizing scanning electron micrographs of longitudinal LLN sections, nucleus-to-nucleus distances ranged between 1 and 200  $\mu\text{m}$ , implying considerably variable spatial organization of ensheathing glia.

To assess the cellular identity of the ensheathing cells at the molecular level, we performed FISH on LLNs with probes for SOXE transcription factors, frequently used markers of the neural crest-derived Schwann cell lineage (McCauley and Bronner-Fraser, 2006; Stolt and Wegner, 2010; Cattell et al., 2012; Li and Richardson, 2016; Tai et al., 2016). Indeed, the probes for lamprey *SoxE2* and *SoxE3*-mRNAs, orthologs of mammalian *Sox10* and *Sox9* (Uy et al., 2012), displayed labeling in ensheathing cells (Fig. 3E). The probe for lamprey *SoxE1* (the ortholog of mammalian *Sox8*) did not yield specific FISH labeling. Together, these results indicate that ensheathing cells in the lamprey PNS are orthologs of mammalian Schwann cells.

To characterize the morphology of the ensheathing cells in 3D, we performed FIB-SEM of the LLNs. When reconstructing the adaxonal and abaxonal plasma membranes of an ensheathing cell over a depth of  $\geq 20 \mu\text{m}$  (Fig. 3F, Movie 1), its morphology was largely homogenous. Likewise, a bundle of several axons (Fig. 3G, Movie 2) was largely regular over  $\geq 20 \mu\text{m}$ . However, as an anecdotal finding, we observed one axon leaving its bundle (Fig. 3H). As exemplified in Figure 3I, small-caliber LLN axons were frequently bundled in a unit of two or more axons (Fig. 4C,E) and one or more ensheathing cell processes (Fig. 4D,F) covered by a

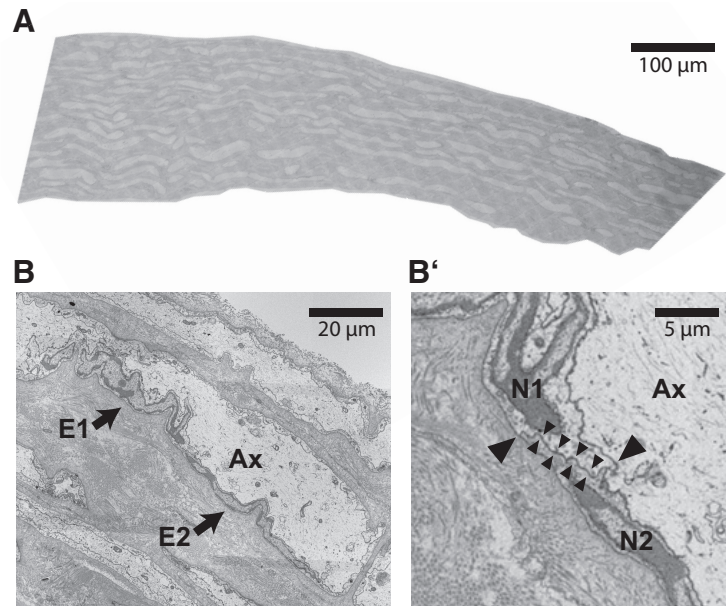


**Figure 5.** Continuous longitudinal ensheathment of axons in the lamprey PNS. **A**, Scanning electron micrograph of a longitudinally sectioned LLN of an adult lamprey. **B**, Higher magnification to exemplify a segment of a longitudinally sectioned axon (Ax) with two adjacent ensheathing cells (arrows pointing at E1, E2). **B'**, Magnification from **B** to highlight the cell-to-cell contact between the ensheathing cells as identified by their nuclei (N1, N2). Large arrowheads point at the adaxonal and the abaxonal surfaces of the contact between the neighboring ensheathing cells. Note the direct apposition of their plasma membranes (small arrowheads). One representative of  $n = 27$  contacts between longitudinally adjacent ensheathing glia in one adult lamprey is shown. Note that ensheathment gaps reminiscent of mammalian nodes of Ranvier were not observed, suggesting that glial ensheathment is largely continuous along peripheral lamprey axons.

basal lamina. Most axons in bundles displayed calibers between 0.3  $\mu\text{m}$  and 1.7  $\mu\text{m}$ , yet some axonal calibers reached up to 3  $\mu\text{m}$  (Fig. 3J).

Using FIB-SEM and 3D reconstruction, ensheathment gaps reminiscent of mammalian nodes of Ranvier were not evident. To assess whether the ensheathment of peripheral axons by glial cells is indeed continuous, we used SEM to analyze longitudinally sectioned adult LLNs at high resolution. As exemplified in Figure 5, longitudinally adjacent ensheathing cells displayed immediate contact via direct apposition of their plasma membranes. Node-like ensheathment gaps or contacting microvilli were not observed. Therefore, glial ensheathment of peripheral lamprey axons is largely continuous, at least in the adult LLN.

To examine axon–glia units in the lamprey CNS, we subjected entire cross-sectioned SCs (Fig. 6A,B) to SEM (Fig. 6C). The SC is approximately four times larger in adult compared with larval lamprey, reflecting maturation-dependent growth. When assessing the 18 ventral giant axons, their calibers were approximately doubled in adult SC (Fig. 6D') compared with larval SC (Fig. 6D). The frequency distributions of axonal calibers in the lateral and dorsal SC (Fig. 6B') shifted toward large-caliber axons in adult SC (Fig. 6E',F') compared with larval SC (Fig. 6E,F) (Kolmogorov–Smirnov test  $p < 0.0001$ ). Therefore, SC axons display considerable maturation-dependent radial growth.

Closer examination showed that SC axons are covered to a variable degree but rarely completely ensheathed by glial processes (Fig. 7A,A',B). The degree of ensheathment was not evidently related to axonal calibers (Fig. 7B). The processes generally displayed dense intermediate filaments, glycogen particles, and desmosomes (Fig. 7C,C',D), ultrastructural features of astrocytes. When detecting the lamprey ortholog of the astrocyte marker *Aldh1l1* (Cahoy et al., 2008) by FISH, many glial cells in the SC displayed robust labeling (Fig. 7E–G).

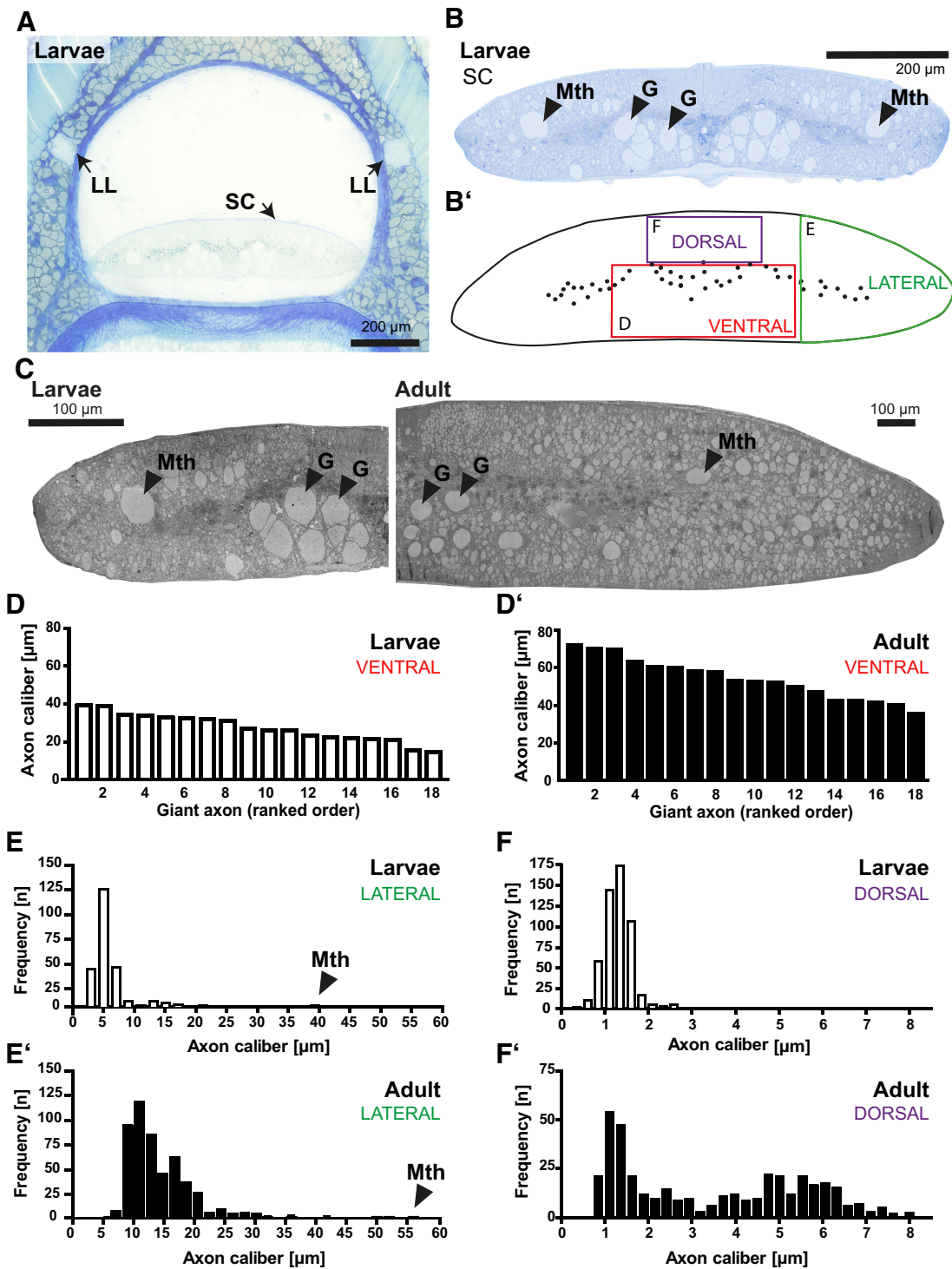


**Figure 6.** Maturation-dependent radial growth of central lamprey axons. **A**, Micrograph of a semithin-sectioned larval body piece stained with methylene blue and Azure II. SCs and LLNs are indicated. **B, B'**, Magnification of the larval SC (**B**) and scheme (**B'**) to illustrate regions selected for quantification of axonal calibers in the ventral, lateral, and dorsal SC (red, green, and purple boxes, respectively). Arrowheads point at giant reticulospinal axons (G) and Mauthner axons (Mth). **C**, Scanning electron micrograph of the larval (left) and adult (right) SC illustrating maturation-dependent growth. Displayed is one half SC each. Note the different scale bar sizes. **D, D'**, Calibers of the 18 giant reticulospinal axons in the ventral SC of larval (**D**) and adult (**D'**) lamprey.  $n = 18$  giant axons each in 1 larvae and 1 adult. **E, E'**, Axonal calibers in the lateral SC of larval (**E**) and adult (**E'**) lamprey. Arrowheads point at values for giant Mauthner axons (Mth).  $n = 239$  axons in 2 larvae;  $n = 500$  axons in 1 adult. **F, F'**, Axonal calibers in the dorsal SC of larval (**F**) and adult (**F'**) lamprey.  $n = 510$  axons in 2 larvae;  $n = 449$  axons in 1 adult. Note the maturation-dependent radial growth of axons in all analyzed SC regions.

To assess their spatial organization, we performed FIB-SEM of the SC (Fig. 7H). 3D reconstruction revealed considerable cellular branching. Both cell bodies and primary processes contained large lipid droplets (Fig. 7H', Movie 3).

This implies that the axon-covering glial cells in the lamprey CNS are orthologs of astrocytes. Cells morphologically resembling oligodendrocyte progenitor cells or mature oligodendrocytes were not found.



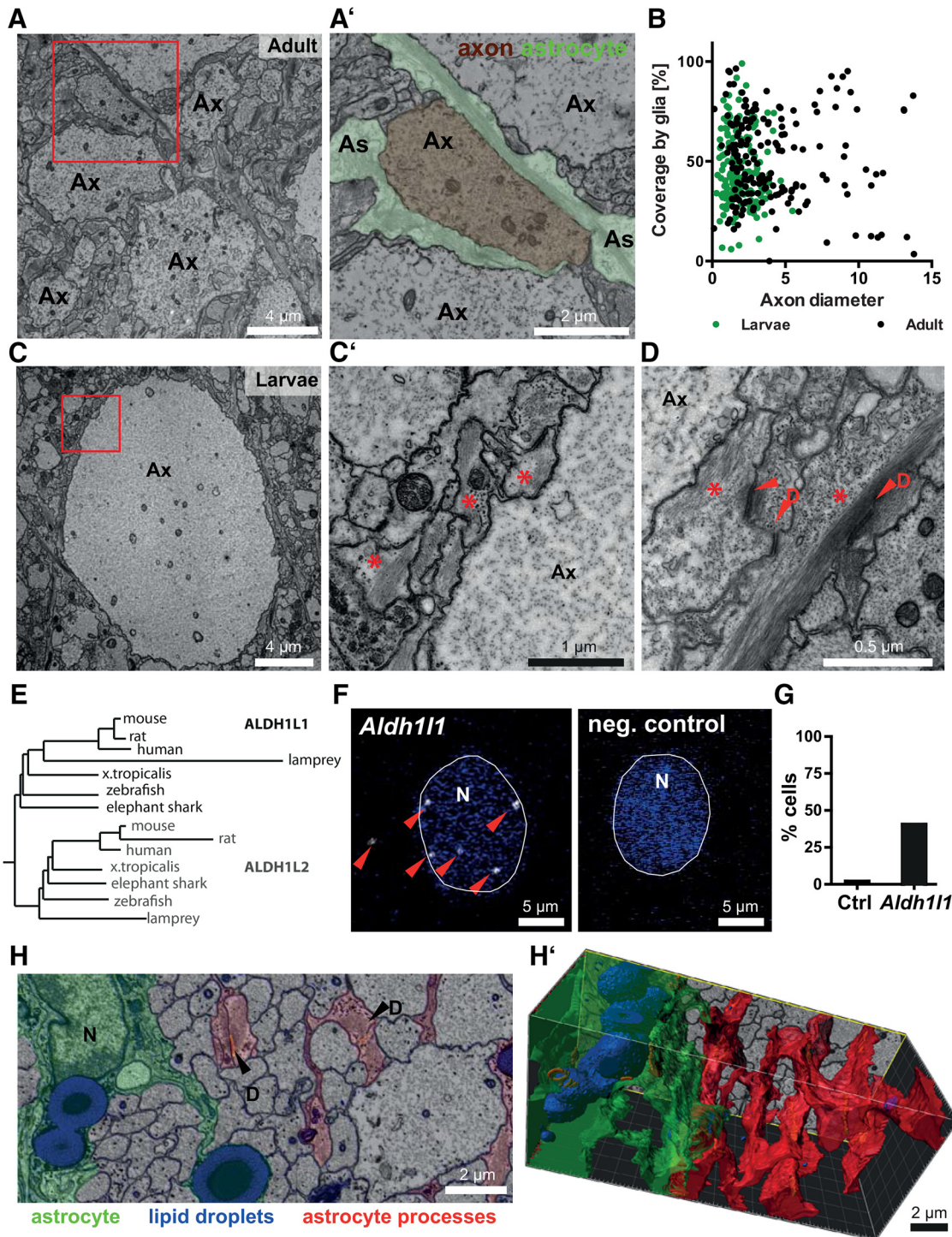
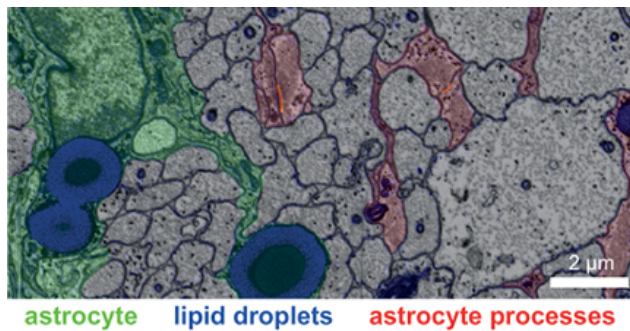


**Figure 7.** Axonal coverage by astrocyte orthologs in the lamprey CNS. **A**, Electron micrograph of the dorsal SC in adult lamprey. The red box is magnified in **A'**. **A'**, Magnification of an axon (Ax) pseudocolored in brown to highlight its coverage by glial processes (As; green). **B**, Coverage of axonal surface with glial processes. Coverage of axonal surface with glial processes in the larval (green data points) and adult (black data points) SC plotted against axonal caliber.  $n = 199$  axons in 2 larvae;  $n = 175$  axons in 1 adult. Note that there is no evident correlation between axonal coverage and caliber. **C**, Electron micrograph of the dorsal SC in larval lamprey. The red box is magnified in **C'**. **C'**, Magnification of an axon (Ax) and glial processes to highlight that the glial cells display a high density of intermediate filaments and glycogen-particles (red stars). **D**, Desmosomes (D) were also frequent. Note that a high density of intermediate filaments, glycogen particles, and desmosomes are ultrastructural features of astrocytes. **E**, Sequence relationships of the astrocyte marker ALDH1L1 and the related ALDH1L2 in a phylogenetic tree. Note that lamprey ALDH1L1 clusters together with its orthologs in other species. **F**, FISH of lamprey SC with probes specific for lamprey *Aldh11* or a negative control (*E. coli Kd12*). Maximum intensity projection images showing *Aldh11* labeling (pseudocolor representation in white) in proximity to nuclei (N) (DAPI, blue). **G**, A considerable portion of cells displayed *Aldh11* labeling in the adult SC.  $n = 198$  DAPI-positive cells in 1 adult lamprey. **H**, **H'**, FIB-SEM micrograph (**H**) of the dorsal larval SC and 3D reconstruction (**H'**). A glial cell body and its primary processes are pseudocolored in green; large lipid droplets are pseudocolored in blue. Glial processes not connected to that cell are highlighted in red. D, Desmosome. See also Movie 3.



**Movie 3.** Association of axons and glial cells in the SC. FIB-SEM of the dorsal larval SC and 3D reconstruction. A glial cell body and its primary processes are pseudocolored in green; large lipid droplets are pseudocolored in blue. Glial processes not connected to that cell are highlighted in red. For preview image, see Figure 7H.



## Discussion

We assessed the structural organization of axon–glia units in sea lamprey, a model for jawless vertebrates (agnathans) that diverged from jawed vertebrates before the evolutionary emergence of myelin in the latter. Our optimized sample preparation with en bloc contrasting using osmium-thiocarbohydrazide-osmium (Deerinck et al., 2010) may also facilitate electron microscopy of nervous system morphology in other aquatic species, for which excellent tissue preservation and contrast are not routinely achieved.

When comparing larval and adult lamprey, axonal calibers increase markedly in both PNS and CNS. Considering that nerve conduction velocity is proportional to axon caliber (Rushton, 1951), this increase appears suited to accelerate conduction after transformation from comparatively sedentary larva into adults that require efficient locomotion control (McClellan et al., 2016). Both large calibers and myelination of axons facilitate rapid impulse propagation. However, conduction velocity along myelinated axons is squared compared with unmyelinated axons of the same caliber but only proportional to the square root of axonal caliber (Hartline and Colman, 2007). Myelination thus allows rapid conduction along many axons with very limited space requirements, a relevant feature of nervous systems in jawed vertebrates. We hypothesize that myelination, but not ensheathment, restricts radial growth of axons. However, whether myelin restricts axonal calibers by mechanic constraints, molecular cues, or both is unknown.

Peripheral ensheathing glia in lamprey share many characteristics with mammalian Schwann cells, including expression of *SoxE* transcription factors (McCauley and Bronner-Fraser, 2006; Stolt and Wegner, 2010; Tai et al., 2016), coverage by a basal lamina, complete ensheathment of all peripheral axons, and the existence of an axonal threshold caliber for their exclusion from bundles (Feltri et al., 2016). Together, morphological and molecular criteria imply that peripheral ensheathing glia in lamprey are orthologs of mammalian nonmyelinating Schwann cells; that is, Remak-type Schwann cells.

The maximum caliber of lamprey axons in bundles (3  $\mu\text{m}$ ) is larger and less rigorous than the threshold caliber of mammalian axons (1  $\mu\text{m}$ ) to be sorted out of Remak bundles radially. Interestingly, radial sorting of axons is primarily viewed as the morphogenetic prerequisite for their myelination (Feltri et al., 2016). However, we find that the exclusion of large-caliber axons from bundles for individual ensheathment predates myelin evolution. Radial sorting is thus not necessarily coupled to myelination, implying that it serves additional, possibly metabolic functions.

In the CNS, lamprey axons are also associated with glial cells, which are orthologs of mammalian astrocytes according to *Aldh1l1* expression and intermediate filament density. They also comprise glycogen particles and lipid droplets, which are key to axon–glia metabolic cooperation. Breakdown of glial glycogen into glucose enables the transfer of glycolysis products as fuel for neuronal mitochondria (Fünfschilling et al., 2012; Lee et al., 2012; Volkenhoff et al., 2015), whereas glial lipid droplets are derived from neuronal lipids, at least in flies (Liu et al., 2017). It is tempting to speculate that oligodendrocytes may have evolved in ancient gnathostomata from ancestral glial progenitors with astrocyte-like properties into cells that store neuron-derived lipids as myelin constituents rather than lipid droplets (Nave et al., 2017). Less speculatively, the long-term integrity of axons necessitates their metabolic cooperation with Schwann cells, oligodendrocytes, and astrocytes in mammals and ensheathing glia in flies (Fünfschilling et al., 2012; Lee et al., 2012; Beirowski et al., 2014; Volkenhoff et al., 2015; Schirmeier et al., 2016; Liu et al., 2017). The close association of lamprey axons with orthologs of Schwann cells and astrocytes implies that the metabolic support of axons is an ancestral function of glial cells that predates the evolution of myelin.

## References

- Banerjee S, Bhat MA (2008) Glial ensheathment of peripheral axons in *Drosophila*. *J Neurosci Res* 86:1189–1198. [CrossRef Medline](#)
- Bartels M, Krenkel M, Cloetens P, Möbius W, Salditt T (2015) Myelinated mouse nerves studied by X-ray phase contrast zoom tomography. *J Struct Biol* 192:561–568. [CrossRef Medline](#)
- Beirowski B, Babetto E, Golden JP, Chen YJ, Yang K, Gross RW, Patti GJ, Milbrandt J (2014) Metabolic regulator LKB1 is crucial for Schwann cell-mediated axon maintenance. *Nat Neurosci* 17:1351–1361. [CrossRef Medline](#)
- Bertolini B (1964) Ultrastructure of the spinal cord of the lamprey. *J Ultrastruct Res* 11:1–24. [CrossRef Medline](#)
- Brodin L, Shupliakov O (2006) Giant reticulospinal synapse in lamprey: molecular links between active and periaxonal zones. *Cell Tissue Res* 326:301–310. [CrossRef Medline](#)
- Bullock TH, Moore JK, Fields RD (1984) Evolution of myelin sheaths: both lamprey and hagfish lack myelin. *Neurosci Lett* 48:145–148. [CrossRef Medline](#)
- Busch DJ, Morgan JR (2012) Synuclein accumulation is associated with cell-specific neuronal death after spinal cord injury. *J Comp Neurol* 520:1751–1771. [CrossRef Medline](#)
- Cahoy JD, Emery B, Kaushal A, Foo LC, Zamanian JL, Christopherson KS, Xing Y, Lubischer JL, Krieg PA, Krupenko SA, Thompson WJ, Barres BA (2008) A transcriptome database for astrocytes, neurons, and oligodendrocytes: a new resource for understanding brain development and function. *J Neurosci* 28:264–278. [CrossRef Medline](#)
- Castelfranco AM, Hartline DK (2016) Evolution of rapid nerve conduction. *Brain Res* 1641:11–33. [CrossRef Medline](#)
- Cattell MV, Garnett AT, Klymkowsky MW, Medeiros DM (2012) A maternally established SoxB1/SoxF axis is a conserved feature of chordate germ layer patterning. *Evol Dev* 14:104–115. [CrossRef Medline](#)
- Cornide-Petronio ME, Ruiz MS, Barreiro-Iglesias A, Rodicio MC (2011) Spontaneous regeneration of the serotonergic descending innervation in the sea lamprey after spinal cord injury. *J Neurotrauma* 28:2535–2540. [CrossRef Medline](#)
- Deerinck TJ, Bushong EA, Lev-Ram V, Shu X, Tsien RY, Ellisman MH (2010) Enhancing serial block-face scanning electron microscopy to enable high resolution 3-D nanohistology of cells and tissues. *Microscopy and Microanalysis* 16:1138–1139. [CrossRef](#)
- Feltri ML, Poitelon Y, Previtali SC (2016) How Schwann cells sort axons: new concepts. *Neuroscientist* 22:252–265. [CrossRef Medline](#)
- Fernández-López B, Valle-Maroto SM, Barreiro-Iglesias A, Rodicio MC (2014) Neuronal release and successful astrocyte uptake of aminoacidic neurotransmitters after spinal cord injury in lampreys. *Glia* 62:1254–1269. [CrossRef Medline](#)

- Fraher J (2002) Axons and glial interfaces: ultrastructural studies. *J Anat* 200:415–430. [CrossRef Medline](#)
- Freeman MR (2015) *Drosophila* central nervous system glia. *Cold Spring Harb Perspect Biol* 7:a020552. [CrossRef Medline](#)
- Fünfschilling U, Supplie LM, Mahad D, Boretius S, Saab AS, Edgar J, Brinkmann BG, Kassmann CM, Tzvetanova ID, Möbius W, Diaz F, Meijer D, Suter U, Hamprecht B, Sereda MW, Moraes CT, Frahm J, Goebbels S, Nave KA (2012) Glycolytic oligodendrocytes maintain myelin and long-term axonal integrity. *Nature* 485:517–521. [CrossRef Medline](#)
- Gelman S, Cohen AH, Sanovich E (2009) Developmental changes in the ultrastructure of the lamprey lateral line nerve during metamorphosis. *J Morphol* 270:815–824. [CrossRef Medline](#)
- Gerachshenko T, Schwartz E, Bleckert A, Photowala H, Seymour A, Alford S (2009) Presynaptic G-protein-coupled receptors dynamically modify vesicle fusion, synaptic cleft glutamate concentrations, and motor behavior. *J Neurosci* 29:10221–10233. [CrossRef Medline](#)
- Green SA, Uy BR, Bronner ME (2017) Ancient evolutionary origin of vertebrate enteric neurons from trunk-derived neural crest. *Nature* 544:88–91. [CrossRef Medline](#)
- Grillner S, El Manira A (2015) The intrinsic operation of the networks that make us locomote. *Curr Opin Neurobiol* 31:244–249. [CrossRef Medline](#)
- Grillner S, Robertson B (2016) The basal ganglia over 500 million years. *Curr Biol* 26:R1088–R1100. [CrossRef Medline](#)
- Hartline DK, Colman DR (2007) Rapid conduction and the evolution of giant axons and myelinated fibers. *Curr Biol* 17:R29–R35. [CrossRef Medline](#)
- Hill AS, Nishino A, Nakajo K, Zhang G, Fineman JR, Selzer ME, Okamura Y, Cooper EC (2008) Ion channel clustering at the axon initial segment and node of Ranvier evolved sequentially in early chordates. *PLoS Genet* 4:e1000317. [CrossRef Medline](#)
- King B, Qiao T, Lee MSY, Zhu M, Long JA (2017) Bayesian morphological clock methods resurrect placoderm monophyly and reveal rapid early evolution in jawed vertebrates. *Syst Biol* 66:499–516. [CrossRef Medline](#)
- Knott G, Marchman H, Wall D, Lich B (2008) Serial section scanning electron microscopy of adult brain tissue using focused ion beam milling. *J Neurosci* 28:2959–2964. [CrossRef Medline](#)
- Krenkel M, Markus A, Bartels M, Dullin C, Alves F, Salditt T (2015) Phase-contrast zoom tomography reveals precise locations of macrophages in mouse lungs. *Sci Rep* 5:9973. [CrossRef Medline](#)
- Krüger SP, Neubauer H, Bartels M, Kalbfleisch S, Giewekemeyer K, Wilbrandt PJ, Sprung M, Salditt T (2012) Sub-10 nm beam confinement by X-ray waveguides: design, fabrication and characterization of optical properties. *J Synchrotron Radiat* 19:227–236. [CrossRef Medline](#)
- Lau BY, Fogerson SM, Walsh RB, Morgan JR (2013) Cyclic AMP promotes axon regeneration, lesion repair and neuronal survival in lampreys after spinal cord injury. *Exp Neurol* 250:31–42. [CrossRef Medline](#)
- Lee Y, Morrison BM, Li Y, Lengacher S, Farah MH, Hoffman PN, Liu Y, Tsingalia A, Jin L, Zhang PW, Pellerin L, Magistretti PJ, Rothstein JD (2012) Oligodendroglia metabolically support axons and contribute to neurodegeneration. *Nature* 487:443–448. [CrossRef Medline](#)
- Li H, Richardson WD (2016) Evolution of the CNS myelin gene regulatory program. *Brain Res* 1641:111–121. [CrossRef Medline](#)
- Liu L, MacKenzie KR, Putluri N, Maletić-Savatić M, Bellen HJ (2017) The glia-neuron lactate shuttle and elevated ROS promote lipid synthesis in neurons and lipid droplet accumulation in glia via APOE/D. *Cell Metab* 26:719–737. [e6. Medline](#)
- Lurie DI, Pijak DS, Selzer ME (1994) Structure of reticulospinal axon growth cones and their cellular environment during regeneration in the lamprey spinal cord. *J Comp Neurol* 344:559–580. [CrossRef Medline](#)
- Marin O, Valiente M, Ge X, Tsai LH (2010) Guiding neuronal cell migrations. *Cold Spring Harb Perspect Biol* 2:a001834. [CrossRef Medline](#)
- Martik ML, Bronner ME (2017) Regulatory logic underlying diversification of the neural crest. *Trends Genet* 33:715–727. [CrossRef Medline](#)
- McCauley DW, Bronner-Fraser M (2006) Importance of SoxE in neural crest development and the evolution of the pharynx. *Nature* 441:750–752. [CrossRef Medline](#)
- McClellan AD, Pale T, Messina JA, Buso S, Shebib A (2016) Similarities and differences for swimming in larval and adult lampreys. *Physiol Biochem Zool* 89:294–312. [CrossRef Medline](#)
- Morgan JR, Di Paolo G, Werner H, Shchedrina VA, Pypaert M, Pieribone VA, De Camilli P (2004) A role for talin in presynaptic function. *J Cell Biol* 167:43–50. [CrossRef Medline](#)
- Mullins OJ, Hackett JT, Buchanan JT, Friesen WO (2011) Neuronal control of swimming behavior: comparison of vertebrate and invertebrate model systems. *Prog Neurobiol* 93:244–269. [CrossRef Medline](#)
- Nave KA, Werner HB (2014) Myelination of the nervous system: mechanisms and functions. *Annu Rev Cell Dev Biol* 30:503–533. [CrossRef Medline](#)
- Nave KA, Tzvetanova ID, Schirmeier S (2017) Glial cell evolution: the origins of a lipid store. *Cell Metab* 26:701–702. [CrossRef Medline](#)
- Peters A (1960) The structure of the peripheral nerves of the lamprey (*Lampetra fluviatilis*). *J Ultrastruct Res* 4:349–359. [CrossRef Medline](#)
- Rasmussen JP, Sagasti A (2017) Learning to swim, again: axon regeneration in fish. *Exp Neurol* 287:318–330. [CrossRef Medline](#)
- Richardson KC, Jarett L, Finke EH (1960) Embedding in epoxy resins for ultrathin sectioning in electron microscopy. *Stain Technol* 35:313–323. [CrossRef Medline](#)
- Rovainen CM, Dill DA (1984) Counts of axons in electron microscopic sections of ventral roots in lampreys. *J Comp Neurol* 225:433–440. [CrossRef Medline](#)
- Rushton WA (1951) A theory of the effects of fibre size in medullated nerve. *J Physiol* 115:101–122. [CrossRef Medline](#)
- Salditt T, Osterhoff M, Krenkel M, Wilke RN, Priebe M, Bartels M, Kalbfleisch S, Sprung M (2015) Compound focusing mirror and X-ray waveguide optics for coherent imaging and nano-diffraction. *J Synchrotron Radiat* 22:867–878. [CrossRef Medline](#)
- Salzer JL, Zalc B (2016) Myelination. *Curr Biol* 26:R971–R975. [CrossRef Medline](#)
- Schertel A, Snaidero N, Han HM, Ruhwedel T, Laue M, Grabenbauer M, Möbius W (2013) Cryo FIB-SEM: volume imaging of cellular ultrastructure in native frozen specimens. *J Struct Biol* 184:355–360. [CrossRef Medline](#)
- Schirmeier S, Matzat T, Klämbt C (2016) Axon ensheathment and metabolic supply by glial cells in *Drosophila*. *Brain Res* 1641:122–129. [CrossRef Medline](#)
- Schultz R, Berkowitz EC, Pease DC (1956) The electron microscopy of the lamprey spinal cord. *J Morphol* 98:251–273. [CrossRef](#)
- Schweitzer J, Becker T, Schachner M, Nave KA, Werner H (2006) Evolution of myelin proteolipid proteins: gene duplication in teleosts and expression pattern divergence. *Mol Cell Neurosci* 31:161–177. [CrossRef Medline](#)
- Smith JJ, Kuraku S, Holt C, Sauka-Spengler T, Jiang N, Campbell MS, Yandell MD, Manousaki T, Meyer A, Bloom OE, Morgan JR, Buxbaum JD, Sachidanandam R, Sims C, Garruss AS, Cook M, Krumlauf R, Wiedemann LM, Sower SA, Decatur WA, et al. (2013) Sequencing of the sea lamprey (*Petromyzon marinus*) genome provides insights into vertebrate evolution. *Nat Genet* 45:415–421. [CrossRef Medline](#)
- Stolt CC, Wegner M (2010) SoxE function in vertebrate nervous system development. *Int J Biochem Cell Biol* 42:437–440. [CrossRef Medline](#)
- Sugahara F, Aota S, Kuraku S, Murakami Y, Takio-Ogawa Y, Hirano S, Kuratani S (2011) Involvement of hedgehog and FGF signalling in the lamprey telencephalon: evolution of regionalization and dorsoventral patterning of the vertebrate forebrain. *Development* 138:1217–1226. [CrossRef Medline](#)
- Sugahara F, Murakami Y, Pascual-Anaya J, Kuratani S (2017) Reconstructing the ancestral vertebrate brain. *Dev Growth Differ* 59:163–174. [CrossRef Medline](#)
- Tai A, Cheung M, Huang YH, Jauch R, Bronner ME, Cheah KS (2016) SOXE neofunctionalization and elaboration of the neural crest during chordate evolution. *Sci Rep* 6:34964. [CrossRef Medline](#)
- Tasaki I (1939) The electro-saltatory transmission of the nerve impulse and the effect of narcosis upon the nerve fiber. *Am J Physiol* 127:211–227.
- Uy BR, Simoes-Costa M, Sauka-Spengler T, Bronner ME (2012) Expression of sox family genes in early lamprey development. *Int J Dev Biol* 56:377–383. [CrossRef Medline](#)
- Volkenhoff A, Weiler A, Letzel M, Stehling M, Klämbt C, Schirmeier S (2015) Glial glycolysis is essential for neuronal survival in *Drosophila*. *Cell Metab* 22:437–447. [CrossRef Medline](#)
- Werner HB (2013) Do we have to reconsider the evolutionary emergence of myelin? *Front Cell Neurosci* 7:217. [CrossRef Medline](#)
- Will TJ, Tushev G, Kochen L, Nassim-Assir B, Cajigas JJ, Tom Dieck S, Schuman EM (2013) Deep sequencing and high-resolution imaging reveal compartment-specific localization of Bdnf mRNA in hippocampal neurons. *Sci Signal* 6:rs16. [CrossRef Medline](#)
- Zalc B, Goujet D, Colman D (2008) The origin of the myelination program in vertebrates. *Curr Biol* 18:R511–R512. [CrossRef Medline](#)